https://doi.org/10.5194/egusphere-2025-6328
Preprint. Discussion started: 7 January 2026

Impact of Sentinel-5 SWIR Detector Persistence on Trace Gas Retrievals

Mari C. Martinez-Velarte[1], Jochen Landgraf[1], Ben Veihelmann[2], Bernd Sierk[2,a], and Tobias Borsdorff[1]

[1]SRON Space Research Organization Netherlands
[2]ESA-ESTEC, Noordwijk, The Netherlands
[a]now at: EUMETSAT, Eumetsat Allee 1, 64295 Darmstadt, Germany

Correspondence: Tobias Borsdorff (t.borsdorff@sron.nl)

Abstract. Launched in August 2025, the Sentinel-5 (S5) mission aims to enhance greenhouse gas monitoring by working alongside existing Copernicus satellites, such as the Sentinel-5 Precursor. S5 is equipped with shortwave-infrared (SWIR) grating spectrometers that provide operational daily retrievals of CH_4 and CO, while the coverage of the SWIR region also makes S5 measurements sensitive to atmospheric CO_2. One particular challenge for S5 is the persistence effect in its SWIR mercury-cadmium-telluride (MCT) detectors, which can introduce scene-dependent radiometric biases when the signal at a detector pixel changes between consecutive readouts, as occurs in scenes with along-track brightness variations.

This study quantifies persistence-induced biases for CH_4, CO, and the CH_4/CO_2 proxy ratio using the operational RemoTeC CH_4 retrieval algorithm, an also examines persistence errors for a potential CO_2 product. We simulate realistic scenes over regions like the Nile Delta, California's Central Valley, and the Lusatian lignite district, which exhibit the spatial radiance variability relevant for persistence effects. Across these scenes, the induced biases remain small, with typical amplitudes below 0.12 % for CH_4, 0.10 % for CO_2, 0.34 % for CO, and 0.06 % for the CH_4/CO_2 proxy. However, localized outliers reaching up to 1.59 % for CH_4, 1.55 % for CO_2, 4.01 % for CO and 0.71 % for the proxy constitute a substantial fraction of the CO and the proxy performance targets, and exceed those defined for CH_4 and CO_2. Our findings suggest that targeted post-filtering, such as omitting coastal and land–water interface pixels, can effectively reduce the most significant outliers in the persistence bias, thus aligning the retrieval biases with the required mission performance.

1 Introduction

Sentinel-5 (S5) was launched in August 2025 aboard *MetOp-SG-A1*, the first of three MetOp Second Generation (MetOp-SG) A/B satellite pairs intended to deliver over two decades of atmospheric and meteorological observations. The mission serves key applications in air quality, climate, and environmental policy, and ensures the continuity of long-term records within the Copernicus program. It will provide near-daily global coverage of atmospheric composition—including trace gases and aerosols—at a spatial sampling of approximately $7.1 \times 7.5\ \mathrm{km}^2$ at nadir (Ingmann et al., 2012; Sierk et al., 2018). The mission's core instrument, the Ultraviolet, Visible, Near-infrared, and Short-wave Infrared (UVNS) spectrometer, is a passive grating imaging spectrometer covering seven spectral bands from $270\ \mathrm{nm}$–$2385\ \mathrm{nm}$ (Irizar et al., 2019). Sentinel-5 overlaps and

https://doi.org/10.5194/egusphere-2025-6328
Preprint. Discussion started: 7 January 2026

complements its predecessor, Sentinel-5 Precursor (S5P), enabling cross-calibration and complementary orbit sampling due to their different local overpass times (in the early morning for S5 and in the early afternoon for S5P). Compared with S5P's TROPOMI spectrometer, S5's UVNS instrument offers a broader spectral range while employing a coarser spatial sampling ($7.1 \times 7.5\ \mathrm{km}^2$ vs. $5.5 \times 7.0\ \mathrm{km}^2$) (Irizar et al., 2019; KNMI, 2022). The extended spectral coverage—including the SWIR-1 band ($1590\,\mathrm{nm}$–$1675\,\mathrm{nm}$) in addition to SWIR-3 ($2305\,\mathrm{nm}$–$2385\,\mathrm{nm}$)—enables sensitivity to CO_2 and CH_4/CO_2 proxy retrievals alongside CH_4 and CO observations. This supports advanced trace-gas and aerosol studies relevant to air-quality and climate applications.

The S5 SWIR channels utilize a Lynred Next-Generation Panchromatic (NGP) HgCdTe (MCT) detector with a dedicated readout circuit (ROIC). NGP represents Lynred's successor line to the Saturn-series detectors flown on TROPOMI. It comprises two architectures: the earlier Advanced MCT Array Module (AMAM), used on Sentinel-5, and the more recent Modular Infrared Array Module (MIAM). In the AMAM architecture, the MCT layer is grown on a CdZnTe substrate before it is chemically etched away and coated with an anti-reflective layer (ARL) (Delannoy et al., 2015). This fabrication step introduces charge trapping/de-trapping mechanisms at the MCT/ARL interface, giving rise to detector persistence (also known as memory or lag effect). The delayed release of these charges adds an unwanted current in subsequent frames, producing scene-dependent radiometric deviations. Such deviations become particularly relevant when the incident signal varies between successive readouts, as encountered in scenes with strong along-track brightness variations. To address this issue, Lynred developed the MIAM architecture, which significantly mitigates the trapping/de-trapping effects. This enhanced architecture is employed within the Copernicus CO2M mission (Sierk et al., 2021). However, upgrading the Sentinel-5 detector from AMAM to MIAM was not feasible due to technical and programmatic constraints. Consequently, the Sentinel-5 AMAM detector must contend with persistence arising from both the charge trapping/de-trapping and other memory-related effects—such as those originating from the ROIC—that persist across all NGP architectures.

Accurate mitigation of the AMAM detector's charge-trapping component is required and draws upon heritage from similar missions. In CNES MicroCarb, which also employs the AMAM architecture (Pasternak et al., 2017), the complexity of modeling and correcting persistence effects motivated the adoption of a hardware-based mitigation strategy based on a trap-flooding method (McLeod and Smith, 2016). Building on this foundation, the present effort is focused on characterizing the AMAM detector's charge trapping/de-trapping behavior and quantifying the associated radiometric biases in Level-2 products. This study extends the CNES persistence model—originally developed for preliminary MicroCarb assessments— to achieve this goal. ROIC-induced lag effects are not addressed in the present study.

Using the CNES persistence model, we aim to demonstrate the expected S5 mission performance accounting for persistence-induced errors in the SWIR-1 and SWIR-3 spectral bands. We discuss the errors in the context of the mission science requirements: $1.0\,\%$ uncertainty for CH_4 retrievals and $4\times10^{17}\ \mathrm{molecules\,cm^{-2}}$ for CO, which corresponds to $20\,\%$ of a typical column of $2\times10^{18}\ \mathrm{molecules\,cm^{-2}}$ (European Space Agency (ESA), 2020). Additionally, we consider the performance target of $0.5\,\%$ for CO_2, which is not an operational data product of S5 but of high scientific relevance. For context, dedicated CO_2 missions such as MicroCarb and CO2M adopt more stringent accuracy requirements for XCO_2 (of $0.4\,\mathrm{ppm}$, corresponding to approximately $0.1\,\%$), which makes it particularly relevant to assess persistence effects on CO_2 the present analysis.

https://doi.org/10.5194/egusphere-2025-6328
Preprint. Discussion started: 7 January 2026

To this end, we perform an simulated-based experiment in which synthetic top-of-atmosphere radiances are generated and perturbed by the persistence signal using the CNES model. Subsequently, CH_4, CO, and CO_2 are retrieved with RemoTeC algorithm (Butz et al., 2010), which is used for the operational S5 CH_4 retrieval. By comparing perturbed and unperturbed (ideal) retrievals, we assess the impact of persistence signal on XCH_4, XCO_2, and XCO, including the CH_4/CO_2 proxy approach. The analysis covers controlled synthetic scenes with a binary albedo transition in flight direction as well as realistic heterogeneous surfaces derived from Sentinel-2A data, representative of diverse land-cover and illumination conditions. Our results show that the persistence effect can introduce notable retrieval biases, particularly over dark or highly variable surfaces such as coastal or water-land interfaces, but that filtering these regions restores accuracy within S5 mission requirements.

The following sections describe the analysis conducted in this study. Section 2 introduces the CNES persistence model and the experiment framework used to assess detector persistence effects. Section 3 presents the outcomes of the persistence simulations, including the analysis of synthetic step-like albedo scenes and realistic cases based on Sentinel-2 albedo data. Finally, Section 4 summaries our findings and discusses their implications for the S5 mission.

2 Methodology

To assess the impact of the persistence effect arising from trapping/de-trapping, we designed an experiment based on synthetic S5 Earth radiance scenes, as illustrated in Figure 1. The radiance scenes were generated by a Level-1B (L1B) scene generator for a single observation geometry over a heterogeneous surface albedo using the approach described in Section 2.1, yielding L1B spectra of the type shown in Figure 2. We generated synthetic radiance scenes averaged to 2.36 km in the across-track (ACT) direction, corresponding to the S5 nadir detector sampling, and to 20 m in along-track (ALT), corresponding to the Sentinel-2 resolution. The synthetic radiances approximate detector-level signals at each readout and served as input to the persistence-effect simulation, where CNES model (Section 2.2) applies a temporal sampling of the incoming signal. The output of the CNES model—referred to hereafter as *perturbed radiance*—represents the synthetic radiance modified by the persistence effect, and is mapped on the 2.36×2.50 km^2 ACT/ALT grid cells. The persistence effect is applied exclusively to the SWIR bands, as the NIR band does not exhibit persistence and is therefore not perturbed in this experiment. For S5, L1B data are provided on a 7.1×7.5 km^2 ACT/ALT grid, resulting from an across-track spatial binning of detector pixels and a temporal co-adding in the along-track direction (both by a factor of 3). Accordingly, the perturbed radiances were then spatially co-added by the same factors in both ACT and ALT directions to map them onto the nominal S5 L1B spatial grid. These radiance scenes were then input to the Level-2 retrieval CH_4 algorithm (Section 2.3). Finally, Level-2 retrievals derived from radiances with perturbed SWIR inputs were compared with those obtained from unperturbed radiances, and the resulting differences were assessed against the S5 mission product requirements.

https://doi.org/10.5194/egusphere-2025-6328
Preprint. Discussion started: 7 January 2026

2.1 Simulation of Synthetic S5 Earth radiance

We constructed a heterogeneous S5 radiance scene from synthetic radiance spectra over spatially varying surface albedo, designed to represent conditions under which the persistence effect becomes relevant. The synthetic S5 radiance spectra were generated for a single observation geometry using RemoTeC.

2.1.1 Albedo maps

Two types of surface albedo scenes were used: one based on Sentinel-2A albedo data representing real-world surface variability, and another consisting of synthetically generated binary patterns designed to mimic idealized albedo discontinuities. In the synthetic case, the scene features a sharp transition in surface reflectance at its center in the along-track (ALT) direction, simulating a discontinuity from a darker to a brighter surface. This scenario mimics a satellite overpass moving from a low-albedo region into a high-albedo one, and we refer to it as the dark-to-bright-albedo (D2B) case. The reverse configuration, representing a transition from a bright to a dark surface, is also considered and referred to as the bright-to-dark (B2D) case. The specific albedo values used to construct the corresponding radiance fields are introduced in the following section. The discontinuous albedo scenes offer a controlled framework for examining the spatial propagation of persistence-induced perturbations.

We also analyze a more realistic albedo scene constructed from Sentinel-2A surface-albedo imagery using bands 6, 7, 11, and 12 (European Space Agency, 2023). Bands 6 and 7, centered at $740\,\mathrm{nm}$ ($\pm 14\,\mathrm{nm}$) and $783\,\mathrm{nm}$ ($\pm 20\,\mathrm{nm}$), respectively, are spectrally averaged to approximate the S5 NIR band. Bands 11 and 12, centered at $1610\,\mathrm{nm}$ ($\pm 90\,\mathrm{nm}$) and $2190\,\mathrm{nm}$ ($\pm 180\,\mathrm{nm}$), are used to represent the SWIR-1 and SWIR-3 spectral windows of Sentinel-5, respectively. Despite the small spectral mismatch with the Sentinel-5 bands, the relative spatial variations in surface reflectance are well represented in the available Sentinel-2 bands. Any resulting albedo differences are minor and are not expected to affect the outcomes of this study.

Three study regions were selected to capture a range of surface heterogeneity and potential trace gas variability: the Nile Delta, California's Central Valley, and the Lusatian lignite district in Eastern Germany. The corresponding Sentinel-2 albedo scenes for these regions are shown in Figure 3. Selection criteria included surface albedo variability, the presence of strong albedo gradients, and proximity to known or potential sources of trace gas emissions.

2.1.2 Synthetic S5 radiance spectrum

We simulated radiance spectra for a given set of atmospheric conditions, such as profiles of trace gases and aerosols. The accurate modeling of absorption by molecules relies on spectroscopic databases, which provide the absorption cross-section of the target absorber CH_4 as well as of the interfering gases CO, CO_2, H_2O and O_2 (Tran et al., 2006; Rothman et al., 2009; Scheepmaker et al., 2013). In order to construct the synthetic S5 radiance spectra, we used a standard model profile for the trace gases. The synthetic spectra include a mild aerosol load with an aerosol optical thickness of 0.1 at 760 nm, represented by a Gaussian vertical distribution centered near the surface (Butz et al., 2010), and assuming standard size distribution with $r_{\mathrm{eff}} = 4$ (Butz et al., 2011) and optical properties taken from lookup tables (Dubovik et al., 2006). Surface albedo spectral

https://doi.org/10.5194/egusphere-2025-6328
Preprint. Discussion started: 7 January 2026

dependence is modeled as wavelength-independent. The synthetic S5 radiance spectra are generated using the LINTRAN V2.1 forward model implemented in RemoTeC (Schepers et al., 2014) and the simulated line-by-line spectra are convolved with a Gaussian Instrument Spectral Response Function (ISRF), applying a full width at half maximum (FWHM) of $0.4\,\mathrm{nm}$ for the NIR band, $0.25\,\mathrm{nm}$ for the SWIR-1 and SWIR-3 band, in accordance with S5 instrument specifications.

To avoid time-consuming simulations, we assume a constant solar and viewing geometry over the entire scenes (solar zenith angle of 50 degree, viewing zenith angle of 0 degree, and relative azimuth angle of 0 degree). A lookup table of spectra is generated for albedo range 0.001-0.63 in steps of 0.003 for the NIR, 0.0002-0.76 in steps of 0.0038 for the SWIR-1, and 0.0006-0.7 in steps of 0.0035 for the SWIR-3. For each pixel in the albedo scene, the corresponding spectra is obtained by selecting from the LUT the entry with the closest albedo value.

2.2 The Persistence Effect Simulator

To quantify the persistence effect, the French Space Agency CNES has developed a model to simulate the effect of charge trapping/de-trapping on the MicroCarb measurements (Jouglet et al., personal communication). Although the model was originally developed for MicroCarb, it can be adapted to represent the behavior of the S5 SWIR detectors, which employ the same underlying detector architecture. The tool models the time-dependent detector response to the input radiance scene and produces a modified radiance spectrum that includes the persistence perturbations.

To assess the persistence effect in Sentinel-2 albedo scenes, we begin by determining the temporal variation of radiances illuminating the instrument. With the Sentinel-2 pixel size in the along-track (ALT) direction, and the satellite's ground speed, we assign a timestamp to each extracted spectrum as described in Sec. 2.1.2. Subsequently, we estimate the detector's current and integrate it along the track over the S5 dwell time. We then calculate the spectrum perturbation by electron trapping current based on the available trap capacity, while the de-trapping current is characterized by an exponential release of charge over time. The persistence effect is quantified by the difference between the trapping and de-trapping currents relative to the unperturbed signal. Consequently, the perturbed radiance scene is initially computed on the S5 detector pixel grid and subsequently, radiances are aggregated onto the S5 co-added pixel grid, which is $7.1 \times 7.5\ \mathrm{km}^2$. Further details of the persistence model are elaborated in appendix A. The resulting spectra are subsequently utilized as input for the RemoTeC retrieval algorithm. Since a different detector is employed, the persistence effect does not impact the NIR band, limiting the computation of the persistence current to the SWIR-1 and SWIR-3 bands.

The co-adding of data when going from the detector grid to the L1B spatial grid can influence the quantification of the persistence-effect-induced bias. This becomes clear when studying the synthetic albedo test cases, where the position of the albedo discontinuity relative to the co-added grid can significantly affect the magnitude of the persistence bias. Section 3.1 examines the sensitivity of the retrieval to this alignment by estimating the errors introduced by shifting the albedo discontinuity with respect to the S5 co-added grid.

https://doi.org/10.5194/egusphere-2025-6328
Preprint. Discussion started: 7 January 2026

2.3 Retrieval of CH_4, CO_2, and CO

The perturbed Earth radiance spectra serve as input to the RemoTeC algorithm, the retrieval code used for the operational Sentinel-5 CH_4 product, which is also used to infer CO_2 and CO trace gases. RemoTeC employs a scattering/non-scattering radiative transfer model to invert the measured spectra and retrieve atmospheric composition. It simulates radiance spectra which are iteratively fitted to observations using a non-linear least-squares optimization, minimizing the difference between simulated and measured spectra (Butz et al., 2010; Schepers et al., 2014).

Aerosol and cirrus scattering represent major challenges for methane retrieval from space-based backscatter measurements in the SWIR range. Retrieval strategies either estimate methane concentrations simultaneously with scattering parameters (full-physics retrieval) or use a proxy approach relying on the CH_4/CO_2 ratio, assuming that scattering effects largely cancel in the ratio and that the background CO_2 field is homogeneous and accurately known from, for example, model data (Schepers et al., 2012).

For our study, we configured the full-physics retrievals (Butz et al., 2011, 2012) to utilize reflectance measurements in the SWIR-1 and SWIR-3 bands (1590–1675 nm and 2305–2385 nm, respectively). Additionally, the NIR band (745 nm to (numerical range) 773 nm) is used to constrain atmospheric scattering properties. Since the SWIR-1 band is sensitive to CO_2 and H_2O absorption, and SWIR-3 is sensitive to CO and H_2O, the total column of these interfering absorbers is also retrieved alongside CH_4 and the surface albedo. Although the operational S5 CO product is based on a different retrieval scheme (SICOR), RemoTeC provides equivalent results within the constraints of this study and, therefore, our CO impact estimates are representative of the operational retrieval.

The proxy retrieval infers the CH_4 proxy product using radiance measurements in the SWIR-1 band under the assumption of a non-scattering atmosphere. The product is defined by

$$\mathrm{XCH_4} = \frac{[\mathrm{CH_4}]}{[\mathrm{CO_2}]}\mathrm{XCO_2^{mod}} \tag{1}$$

where $[CO_2]$ and $[CH_4]$ are retrieved ignoring atmospheric scattering and $\mathrm{XCO_2^{mod}}$ is the dry air column mixing ratio of CO_2 simulated by a model (Frankenberg et al., 2006). Here, the aerosol induced error in $[CO_2]$ and $[CH_4]$ are very similar and cancel out to a large extend in the ratio in Eq. 1.

In summary, we define two retrieval configurations used throughout this work:

Case Proxy: a non-scattering retrieval using SWIR-1, retrieving XCH_4, XCO_2, and H_2O.

Case FP: a full-physics scattering retrieval using NIR, SWIR-1, and SWIR-3, retrieving XCH_4, XCO_2, XCO, and H_2O.

In the proxy retrieval, the output is further used to compute the $[CH_4]/[CO_2]$ ratio directly from the SWIR-1 band, leveraging its concurrent sensitivity to both gases.

Each retrieval case is run under two conditions: an ideal scenario using the unperturbed (ideal) radiance scene, and a perturbed scenario that incorporates the persistence effect. The impact of the persistence effect on the retrievals is quantified

https://doi.org/10.5194/egusphere-2025-6328
Preprint. Discussion started: 7 January 2026

using the *persistence bias*, which we define in relative terms as:

$$\frac{X_{\text{perturbed}} - X_{\text{ideal}}}{X_{\text{ideal}}}, \tag{2}$$

where $X_{\text{perturbed}}$ and X_{ideal} refer to the mean retrieved total columns of the specific trace gas for the perturbed and the ideal case, respectively.

3 Results

3.1 The Binary Albedo Case

We start to quantify the persistence bias using synthetic scenes featuring an abrupt, across-track albedo transition—from albedo A_1 to A_2—located at the center of each scene, with otherwise uniform albedo. This configuration causes the S5 push-broom instrument to experience a rapid temporal change in radiance as it crosses the discontinuity. For each scene, the same albedo values A_1 and A_2 are used in both the SWIR-1 and SWIR-3 bands, while the NIR albedo is set to 1.5 times the corresponding SWIR albedo. This factor was selected to approximate the typical NIR-to-SWIR reflectance ratio found in common land-cover types. Because the maximum magnitude of the persistence bias is expected to depend on both the absolute albedo value and the albedo contrast $(A_2 - A_1)$, we evaluated the simulations across a grid of (A_1, A_2) combinations covering the full range of tested albedos. The results confirm that the persistence-induced bias is negligible in regions of constant albedo, providing a basic sanity check of the model under spatially homogeneous illumination. At the albedo discontinuity, however, pronounced persistence biases occur and persist for several pixels downstream along the track. The persistence length, defined by the distance from the albedo discontinuity to a bias of 0.1%, extends over approximately 1–2 pixels for CH_4 and CO_2, 1–5 pixels for CO, and 1 pixel for the proxy ratio. The largest bias typically appears in the first pixel immediately following the transition, with the effect decaying rapidly in subsequent pixels.

Figure 4 illustrates the dependence of the maximum persistence bias on A_2 for different A_1 values, for CH_4, CO_2, CO and the proxy ratio. All four quantities exhibit similar qualitative behavior. In each case, the largest absolute persistence bias occurs for bright-to-dark (B2D) transitions, with the strongest perturbations found at the lowest A_2 values and the largest albedo contrasts. For the most extreme simulated configuration—(A_1, A_2) = (0.55, 0.05)—the persistence bias reaches -1.74 % for CH_4, -1.32 % for CO_2, -5.45 % for CO, and -0.64 nits% for the proxy. For a given fixed albedo A_1, the persistence bias grows rapidly with increasing albedo contrast in B2D transition scenes but tends to saturate in dark-to-bright (D2B) scenes once the transition exceeds roughly 0.4, with the bias sign reversing from negative to positive.

The magnitude of the persistence effect is also sensitive to the timing of the detector readout relative to the albedo transition, and hence the S5 spatial sampling grid. This sensitivity arises from the along-track integration of the detector signal: when a sharp albedo transition occurs within the integration, the signal accumulates both unperturbed and perturbed radiances. As a result, the net persistence perturbation depends on the sub-pixel position of the albedo transition. This dependence is reflected in the range of persistence biases obtained for different transition positions. For CH_4, biases might range from $0.30\,\%$ to $0.85\,\%$ in D2B and $-1.56\,\%$ to $-0.50\,\%$ in B2D. The proxy CH_4/CO_2 ratio bias exhibits ranges from $0.13\,\%$ to $0.45\,\%$ in D2B and

https://doi.org/10.5194/egusphere-2025-6328
Preprint. Discussion started: 7 January 2026

from $-0.58\,\%$ to $-0.15\,\%$ in B2D (Figure A1). For both CH_4 and the proxy, these variations are significant in the context of the $1.0\,\%$ performance target. For the simulations presented in Figure 4, the discontinuity was placed to yield the maximum persistence bias, providing an upper bound for the expected perturbation.

3.2 S2-Albedo Cases

Here we present the results of the simulated persistence perturbations over three spatially heterogeneous regions: the Nile Delta, California's Central Valley, and the Lusatian district in Eastern Germany. For these simulations, scene surface reflectances were derived from Sentinel-2 albedo data, as described in Section 2.1.2. To account for sensor limitations, pixels below the effective reflectance sensitivity limit (albedo < 0.05) were removed from the statistical evaluation, although they were retained in the persistence perturbation simulations to preserve their influence on the scene. We assess the spatial variability of the resulting persistence bias, its dependence on surface albedo, and the effect of simple filtering strategies on the overall bias statistics.

Figure 5a present the relative persistence CH_4 bias maps for each study region. The spatial patterns reveal that the persistence effect varies strongly with surface heterogeneity. The Nile Delta exhibits pronounced albedo contrasts arising from its diverse land use: dark irrigated croplands and water bodies interspersed with brighter urban areas and desert fringes. In California's Central Valley, the mix of orchards, croplands, fallow fields, wetlands, and urban zones produces strong spatial heterogeneity, with croplands typically showing high NIR and lower SWIR reflectance, dry soils and built areas appearing brighter across bands, and built areas showing moderate reflectance. In contrast, the Lusatian district—dominated by open-pit lignite mines, reclaimed soils, and artificial lakes—shows uniformly lower albedo in the NIR and SWIR, consistent with the prevalence of dark mineral and moist surfaces. These differences in surface type and reflectance are directly reflected in the pixel-level persistence variability and bias statistics. Overall, we find a variability ranging from $0.11\,\%$ to $0.15\,\%$ for CH_4, from $0.08\,\%$ to $0.12\,\%$ for CO_2, from $0.29\,\%$ to $0.40\,\%$ for CO, and from $0.03\,\%$ to $0.06\,\%$ for the proxy ratio. These variations constitute only a small portion of the respective uncertainty budgets ($1.0\,\%$ for CH_4 and the proxy, $0.5\,\%$ for CO_2, and $0.20\,\%$ for CO). Mean biases remain negligible—below $0.02\,\%$ for CH_4 and CO_2, $0.07\,\%$ for CO, and $-0.008\,\%$ for the proxy ratio—confirming that the persistence effect mainly introduces spatial variability rather than a systematic offset. This variability is closely linked to surface reflectance, with lower-albedo surfaces across all spectral bands exhibiting stronger persistence variability, a pattern consistently observed in the Nile Delta, Central Valley, and Lusatian region. Figure 6 quantifies this relationship, showing the dependence of persistence bias on both the absolute SWIR-1 albedo and the pixel-to-pixel albedo gradient (ΔA), using data aggregated from the three regions. The ΔA is defined as the difference between each pixel's albedo and that of the preceding pixel along the along-track direction, consistent with the results in Section 3.1, which showed that persistence signal primarily affects the first pixel following an albedo transition. While most pixels cluster around albedo values of around 0.2 an ΔA between ± 0.05, the largest persistence-induced biases occur for albedo values below 0.2 and for moderate gradients between approximately -0.15 and 0.1. This behavior reflects enhanced detector persistence over darker surfaces, where reduced reflected radiance enhances the relative impact of persistence signal contributions.

Although this variability and overall bias are small, large localized outliers are observed in the three regions, typically located near strong albedo gradients such as coastlines, lakes, or other water-land boundaries. In the Nile Delta, extreme values reach

https://doi.org/10.5194/egusphere-2025-6328
Preprint. Discussion started: 7 January 2026

up to $-1.23\,\%$ for CH_4, $-1.02\,\%$ for CO_2, $-3.52\,\%$ for CO, and $-0.70\,\%$ for the CH_4/CO_2 proxy ratio. These are primarily found along the northern coast, marking the transition between land and the Mediterranean Sea, and around the Faiyum Oasis near Lake Moeris. In California's Central Valley, peak biases occur near the San Francisco Bay–Delta system and around Clear Lake, reaching up to $1.59\,\%$ for CH_4, $1.55\,\%$ for CO_2, $4.01\,\%$ for CO, and $0.71\,\%$ for the proxy ratio. The Lusatian lignite district exhibits only a few outliers in its northwestern part, over the Mecklenburg Lake District, with maximum biases of $1.07\,\%$, $1.28\,\%$, $1.99\,\%$, and $0.61\,\%$ for CH_4, CO_2, CO, and the proxy ratio, respectively. Overall, these outliers represent a substantial fraction of the mission uncertainty budget for CO and the proxy, while exceeding the corresponding targets for CH_4 and CO_2, indicating the need to identify and flag such pixels in operational processing.

To mitigate this issue, we applied an *a posteriori* land-fraction filter to remove pixels partially or fully over water. The land–water mask was derived from the MODIS Water Mask product (MOD44W, version 5; (Carroll et al., 2009)), accessed via Google Earth Engine. The dataset was exported at a spatial resolution of $500\,\mathrm{m}$ and subsequently regridded onto the S5 detector footprint to maintain spatial consistency with the simulated observations. Pixels containing at least $10\,\%$ water coverage were excluded from the analysis. The impact of this filtering is illustrated in Figure 5b and Table 1. The filtered maps show that most large outliers are effectively removed, while both mean and standard deviation of the persistence bias decrease across all regions. The complementary cumulative distributions in Figure 7 further highlight this improvement: the maximum absolute persistence bias is reduced from $1.59\,\%$ to $0.63\,\%$ for CH_4, $1.55\,\%$ to $0.58\,\%$ for CO_2, $4.01\,\%$ to $1.65\,\%$ for CO, and $0.71\,\%$ to $0.26\,\%$ for the proxy ratio. These results demonstrate that a simple *a posteriori* filtering approach, based on land–water fraction, can effectively mitigate the impact of the persistence effect by removing pixels most susceptible to large biases near sharp albedo contrasts. After applying this filter, the remaining biases fall below mission performance requirements for the operational S5 products CH_4 and CO, as well as for the proxy ratio, confirming the robustness of the mitigation strategy. For CO_2, a few isolated pixels still exhibit residual biases slightly above the performance target, suggesting that a refined or gas-specific filtering criterion could further improve its performance.

4 Conclusions

This study quantified the impact of detector persistence on Sentinel-5 CH_4, CO_2, CO, and CH_4/CO_2 proxy retrievals under realistic surface conditions. The persistence effect—caused by charge trapping and de-trapping charges in the SWIR detector—was simulated to assess its propagation into Level-2 trace-gas products. Persistence-induced biases are most pronounced over low-albedo, high-contrast scenes such as lakes, coastal zones, or other mixed water–land pixels. Although mean biases remain small, the maximum localized deviations—$1.59\,\%$ for CH_4, $4\,\%$ for CO, $1.55\,\%$ for CO_2 and $0.71\,\%$ for the proxy—constitute substantial fractions of the CO and proxy uncertainty budget ($20\,\%$, $1\,\%$) and exceed those for CH_4 and CO_2 ($1\,\%$, $0.5\,\%$). These results highlight the need for effective mitigation in operational processing.

The identified persistence-induced biases have important implications for greenhouse-gas retrievals and their downstream use. Uncorrected artifacts may propagate into concentration estimates and flux inversions, affect atmospheric models and data assimilation systems, and reduce consistency between satellite records. They could also bias inter-mission comparisons

https://doi.org/10.5194/egusphere-2025-6328
Preprint. Discussion started: 7 January 2026

and long-term trend analyses if persistent scene-dependent effects remain unaccounted for. It is therefore crucial to develop effective mitigation strategies to ensure the reliability of future Sentinel-5 greenhouse-gas products.

To explore practical mitigation options, we tested a simple *a posteriori* approach based on a land–water mask to evaluate the potential of scene-dependent filtering in reducing persistence-induced artifacts. This approach removed the largest outliers near strong albedo transitions, reducing maximum absolute persistence biases to below the mission performance thresholds for CH_4 and CO, and the proxy ratio, and to near target levels for CO_2. This demonstrates that such masking can substantially limit persistence-induced artifacts in the operational retrievals, providing a practical short-term solution.

Several limitations apply to the present modeling framework. It represents only the trapping/de-trapping processes in the photodiode and omits ROIC-related persistence, which may also contribute to the memory effect, potentially leading to an overall underestimation. The temporal evolution of trapped charge was tuned to laboratory measurements from a MCT detector representative of the S5 SWIR arrays, but trap properties can vary between detectors and evolve over the mission lifetime due to cumulative radiation damage. Despite these uncertainties, the model provides a useful first-order estimate of the Level-2 impact of the memory effect and its dependence on surface albedo.

Future work should validate these findings with in-orbit Sentinel-5 observations and independent reference datasets such as airborne and ground-based campaigns over high-contrast surfaces. Comparisons with other satellite missions (e.g. Sentinel-5P/TROPOMI) will help assess inter-mission consistency and constrain residual biases. Further refinement of the physical modeling of charge trapping and release could improve the representation of photodiode-related persistence, while the ROIC-level effects should be characterized separately and, where possible, corrected through dedicated Level-1 processing strategies such as those explored for CO2M (Gaucel et al., 2023, 2025). For the trapping/de-trapping component, operational or hardware measures—such as trap flooding sequences implemented in the MicroCarb mission—could be evaluated to mitigate persistence at the detector level. Incorporating persistence diagnostics or quality flags into Level-1 processing would further enhance product reliability. These findings provide essential input for assessing the radiometric performance of Sentinel-5 and ensure the traceability and consistency of greenhouse-gas records across current and future missions.

https://doi.org/10.5194/egusphere-2025-6328
Preprint. Discussion started: 7 January 2026

Appendix A: Modeling the persistence effect

The persistence model was originally developed by detector experts at CNES for preliminary MicroCarb studies (Jouglet et al., personal communication). For completeness, we provide here a conceptual overview of the model formulation.

We start with the radiance field convolved with the spectral and ACT instrument response and sampled on ACT detector grid, $I(x_{\mathrm{ACT}}, y_{\mathrm{ALT}}, \lambda)$. The position x_{ACT} indicates the ground position as sampled by the detector, whereas y_{ALT} is the spatial coordinate in-flight direction. For the Sentinel-2 albedo map, the data is sampled each 20 m in both directions. Taking the ground speed of the satellite into account, this spatial sampling can be translated into a temporal sampling of the incoming signal.

The unperturbed signal, i.e. the signal not affected by persistence, is converted to a current as measured by the detector,

$$I_{\mathrm{o}}(t, \lambda) = G_{\mathrm{inst}} I(x_{\mathrm{ACT}}, y_{\mathrm{ALT}}, \lambda). \tag{A1}$$

with the instrument gain

$$G_{\mathrm{inst}} = Q_E \, A \, \Omega \, T \, \Delta\lambda \tag{A2}$$

Here, Q_E is the quantum efficiency describing the efficiency of the photon-to-electron conversion, A is the aperture size, Ω is the solid angle subtended the system's entrance pupil, T the optical transmission of the instrument and $\Delta\lambda$ the spectral sampling of the spectrum.The Sentinel 5 specific numbers are summarized in Tab. A1.

The trapping-detrapping effect is characterized by corresponding currents in the detector. Assuming that at a time t $Q(t)$ charges are trapped by the detector material, the trapping current is proportional to the current I_{det} and the relative difference of $Q(t)$ with respect to a maximum Q_{max}, i.e.

$$I_{\mathrm{trap}}(t) = E_{\mathrm{trap}} \frac{Q_{\mathrm{max}} - Q(t)}{Q_{\mathrm{max}}} I_{\mathrm{o}} \tag{A3}$$

with an efficiency factor E_{trap}. The detrapping current follows an exponential dependence on the number of trapped photons,

$$I_{\mathrm{detrap}}(t) = E_{\mathrm{detrap}} e^{a\, Q(t)} \tag{A4}$$

with empirical constants E_{detrap} and a. Finally, the incremental change in the trapped charges is given by

$$\frac{dQ}{dt}(t) = I_{\mathrm{trap}}(t) - I_{\mathrm{detrap}}(t) \tag{A5}$$

This equation system is integrated over time using $I_{\mathrm{det}}(t)$ and $Q(t = 0) = 0$.

Having derived trapping and detrapping current, the persistence perturbed current is

$$I_{\mathrm{per}}(t) = I_o(t) + \varepsilon \left(I_{\mathrm{trap}}(t) - I_{\mathrm{detrap}}(t) \right) \tag{A6}$$

and the measured signal is proportional to the integral

$$I_{\mathrm{meas}}(t_o) = \frac{1}{G_{\mathrm{inst}} \, t_{\mathrm{dwell}}} \int_{t_o}^{t_o + t_{\mathrm{dwell}}} I_{\mathrm{per}}(t) \tag{A7}$$

where t_{dwell} is the dwell time of the observation. The proportionality is given by the gain G_{inst} times the dwell time t_{dwell}.

https://doi.org/10.5194/egusphere-2025-6328
Preprint. Discussion started: 7 January 2026

Appendix B: Supplementary Results

B1 Synthetic Albedo Cases

Figure A1 shows how the magnitude of the persistence bias varies with the position of the albedo transition within the S5 detector footprint. These results complement the discussion in Sect. 3.1, which highlights the sensitivity of the effect to sub-pixel scene geometry.

B2 Sentinel-2 Albedo Scenes

Figures A2 and A3 show the persistence-induced bias maps for CO_2, CO, and the CH_4/CO_2 proxy ratio over the three study regions, before and after applying the land–water mask, respectively. Figure A4 presents the corresponding albedo-based heatmaps combining data from all regions. These figures complement Figs. 5 and 6 in Sect. 3.2, which focus on CH_4 data, and extend the analysis to the other retrieved gases.

. MCMV, TB and JL provided the RemoTeC algorithm and performed the data analysis. BV developed and provided the persistence simulation tool. MCMV wrote the original draft. All authors contributed to the discussion of the results and to the review and editing of the manuscript.

. The contact author has declared that none of the authors has any competing interests.

. CNES model derived for preliminary MicroCarb studies (Jouglet et al., personal communication).

https://doi.org/10.5194/egusphere-2025-6328
Preprint. Discussion started: 7 January 2026

References

Butz, A., Hasekamp, O. P., Frankenberg, C., Vidot, J., and Aben, I.: CH4 retrievals from space-based solar backscatter measurements: Performance evaluation against simulated aerosol and cirrus loaded scenes, Journal of Geophysical Research: Atmospheres, 115, https://doi.org/https://doi.org/10.1029/2010JD014514, 2010.

Butz, A., Guerlet, S., Hasekamp, O., Schepers, D., Galli, A., Aben, I., Frankenberg, C., Hartmann, J.-M., Tran, H., Kuze, A., Keppel-Aleks, G., Toon, G., Wunch, D., Wennberg, P., Deutscher, N., Griffith, D., Macatangay, R., Messerschmidt, J., Notholt, J., and Warneke, T.: Toward accurate CO2 and CH4 observations from GOSAT, Geophysical Research Letters, 38, https://doi.org/https://doi.org/10.1029/2011GL047888, 2011.

Butz, A., Galli, A., Hasekamp, O., Landgraf, J., Tol, P., and Aben, E.: TROPOMI aboard Sentinel-5 Precursor: Prospective performance of CH4 retrievals for aerosol and cirrus loaded atmospheres, Remote Sensing of Environment, 120, 267–276, https://doi.org/10.1016/j.rse.2011.05.030, 2012.

Carroll, M., Townshend, J., DiMiceli, C., Noojipady, P., and Sohlberg, R.: A new global raster water mask at 250 m resolution, International Journal of Digital Earth, 2, 291–308, https://doi.org/10.1080/17538940902951401, 2009.

Delannoy, A., Fièque, B., Chorier, P., and Riuné, C.: NGP: a new large format infrared detector for observation, hyperspectral and spectroscopic space missions in VISIR, SWIR and MWIR wavebands, in: Sensors, Systems, and Next-Generation Satellites XIX, edited by Meynart, R., Neeck, S. P., and Shimoda, H., vol. 9639, p. 96390R, International Society for Optics and Photonics, SPIE, https://doi.org/10.1117/12.2197239, 2015.

Dubovik, O., Sinyuk, A., Lapyonok, T., Holben, B. N., Mishchenko, M., Yang, P., Eck, T. F., Volten, H., Muñoz, O., Veihelmann, B., van der Zande, W. J., Leon, J.-F., Sorokin, M., and Slutsker, I.: Application of spheroid models to account for aerosol particle nonsphericity in remote sensing of desert dust, Journal of Geophysical Research: Atmospheres, 111, https://doi.org/https://doi.org/10.1029/2005JD006619, 2006.

European Space Agency: Sentinel-2 Level 1 Algorithm Theoretical Baseline Document (ATBD), Tech. Rep. S2-PDGS-MPC-ATBD-L1, European Space Agency (ESA), https://sentiwiki.copernicus.eu/__attachments/1692737/S2-PDGS-MPC-ATBD-L1%20-%20Sentinel-2%20Level%201%20Algorithm%20Theoretical%20Bases%20Document%202023%20-%201.1.pdf, accessed: 2025-05-22, 2023.

European Space Agency (ESA): Sentinel-5: ESA's Polar-orbiting Atmospheric Composition Mission in Support of Copernicus Services, Esa sp-1336, ESA Communications, Noordwijk, The Netherlands, https://www.esa.int/About_Us/ESA_Publications/SP-1336_Sentinel-5_ESA_s_Polar-orbiting_Atmospheric_Composition_Mission_in_Support_of_Copernicus_Services, 2020.

Frankenberg, C., Meirink, J. F., Bergamaschi, P., Goede, A. P. H., Heimann, M., Körner, S., Platt, U., van Weele, M., and Wagner, T.: Satellite chartography of atmospheric methane from SCIAMACHY on board ENVISAT: Analysis of the years 2003 and 2004, Journal of Geophysical Research: Atmospheres, 111, https://doi.org/https://doi.org/10.1029/2005JD006235, 2006.

Gaucel, J.-M., Lefebure, A., Gaucher, A., Bouchage, G., and Sanson, E.: Remanence characterization of NGP detector in SWIR bands, in: International Conference on Space Optics — ICSO 2022, edited by Minoglou, K., Karafolas, N., and Cugny, B., vol. 12777, p. 127772E, International Society for Optics and Photonics, SPIE, https://doi.org/10.1117/12.2689982, 2023.

Gaucel, J.-M., Sierk, B., Glandus, L., Foulon, H., and Soman, M.: Persistance characterization and modeling for CO2M mission, in: International Conference on Space Optics — ICSO 2024, edited by Bernard, F., Karafolas, N., Kubik, P., and Minoglou, K., vol. 13699, p. 136993W, International Society for Optics and Photonics, SPIE, https://doi.org/10.1117/12.3075197, 2025.

https://doi.org/10.5194/egusphere-2025-6328
Preprint. Discussion started: 7 January 2026

Ingmann, P., Veihelmann, B., Langen, J., Lamarre, D., Stark, H., and Courrèges-Lacoste, G. B.: Requirements for the GMES Atmosphere Service and ESA's implementation concept: Sentinels-4/-5 and -5p, Remote Sensing of Environment, 120, 58–69, https://doi.org/10.1016/j.rse.2012.01.023, the Sentinel Missions - New Opportunities for Science, 2012.

Irizar, J., Melf, M., Bartsch, P., Koehler, J., Weiss, S., Greinacher, R., Erdmann, M., Kirschner, V., Albinana, A. P., and Martin, D.: Sentinel-5/UVNS, in: International Conference on Space Optics — ICSO 2018, edited by Sodnik, Z., Karafolas, N., and Cugny, B., vol. 11180, p. 1118004, International Society for Optics and Photonics, SPIE, https://doi.org/10.1117/12.2535923, 2019.

KNMI: TROPOMI Level 1B ATBD: SWIR Detector and Onboard Calibration, Tech. rep., Royal Netherlands Meteorological Institute (KNMI), https://sentinels.copernicus.eu/documents/247904/2476257/Sentinel-5P-TROPOMI-Level-1B-ATBD.pdf/223f9b91-495d-42d0-9136-47488fc430cd, 2022.

McLeod, B. A. and Smith, R.: Mitigation of H2RG persistence with image illumination, in: High Energy, Optical, and Infrared Detectors for Astronomy VII, edited by Holland, A. D. and Beletic, J., vol. 9915, p. 99150G, International Society for Optics and Photonics, SPIE, https://doi.org/10.1117/12.2233083, 2016.

Pasternak, F., Bernard, P., Georges, L., and Pascal, V.: The microcarb instrument, in: International Conference on Space Optics — ICSO 2016, edited by Cugny, B., Karafolas, N., and Sodnik, Z., vol. 10562, p. 105621P, International Society for Optics and Photonics, SPIE, https://doi.org/10.1117/12.2296225, 2017.

Rothman, L., Gordon, I., Barbe, A., Benner, D., Bernath, P., Birk, M., Boudon, V., Brown, L., Campargue, A., Champion, J.-P., Chance, K., Coudert, L., Dana, V., Devi, V., Fally, S., Flaud, J.-M., Gamache, R., Goldman, A., Jacquemart, D., Kleiner, I., Lacome, N., Lafferty, W., Mandin, J.-Y., Massie, S., Mikhailenko, S., Miller, C., Moazzen-Ahmadi, N., Naumenko, O., Nikitin, A., Orphal, J., Perevalov, V., Perrin, A., Predoi-Cross, A., Rinsland, C., Rotger, M., Šimečková, M., Smith, M., Sung, K., Tashkun, S., Tennyson, J., Toth, R., Vandaele, A., and Vander Auwera, J.: The HITRAN 2008 molecular spectroscopic database, Journal of Quantitative Spectroscopy and Radiative Transfer, 110, 533–572, https://doi.org/https://doi.org/10.1016/j.jqsrt.2009.02.013, hITRAN, 2009.

Scheepmaker, R. A., Frankenberg, C., Galli, A., Butz, A., Schrijver, H., Deutscher, N. M., Wunch, D., Warneke, T., Fally, S., and Aben, I.: Improved water vapour spectroscopy in the 4174-4300 cm^{-1} region and its impact on SCIAMACHY HDO/H_2O measurements, Atmospheric Measurement Techniques, 6, 879–894, https://doi.org/10.5194/amt-6-879-2013, 2013.

Schepers, D., Guerlet, S., Butz, A., Landgraf, J., Frankenberg, C., Hasekamp, O., Blavier, J.-F., Deutscher, N., Griffith, D., Hase, F., Kyro, E., Morino, I., Scherlock, V., Sussmann, R., and Aben, E.: Methane retrievals from Greenhouse Gases Observing Satellite (GOSAT) shortwave infrared measurements: Performance comparison of proxy and physics retrieval algorithms, Journal of Geophysical Research. Atmospheres, 117, https://doi.org/10.1029/2012JD017549, 2012.

Schepers, D., aan de Brugh, J., Hahne, P., Butz, A., Hasekamp, O., and Landgraf, J.: LINTRAN v2.0: A linearised vector radiative transfer model for efficient simulation of satellite-born nadir-viewing reflection measurements of cloudy atmospheres, Journal of Quantitative Spectroscopy and Radiative Transfer, 149, 347–359, https://doi.org/https://doi.org/10.1016/j.jqsrt.2014.08.019, 2014.

Sierk, B., Bezy, J.-L., Caron, J., Meynard, R., Veihelmann, B., and Ingmann, P.: The GMES Sentinel-5 mission for operational atmospheric monitoring: status and developments, in: International Conference on Space Optics — ICSO 2012, edited by Cugny, B., Armandillo, E., and Karafolas, N., vol. 10564, p. 1056434, International Society for Optics and Photonics, SPIE, https://doi.org/10.1117/12.2309276, 2018.

Sierk, B., Fernandez, V., Bézy, J.-L., Meijer, Y., Durand, Y., Courrèges-Lacoste, G. B., Pachot, C., Löscher, A., Nett, H., Minoglou, K., Boucher, L., Windpassinger, R., Pasquet, A., Serre, D., and te Hennepe, F.: The Copernicus CO2M mission for monitoring anthropogenic

https://doi.org/10.5194/egusphere-2025-6328
Preprint. Discussion started: 7 January 2026

carbon dioxide emissions from space, in: International Conference on Space Optics — ICSO 2020, edited by Cugny, B., Sodnik, Z., and Karafolas, N., vol. 11852, p. 118523M, International Society for Optics and Photonics, SPIE, https://doi.org/10.1117/12.2599613, 2021.

Tran, H., Flaud, P.-M., Gabard, T., Hase, F., von Clarmann, T., Camy-Peyret, C., Payan, S., and Hartmann, J.-M.: Model, software and database for line-mixing effects in the $\nu 3$ and $\nu 4$ bands of CH4 and tests using laboratory and planetary measurements—I: N2 (and air) broadenings and the earth atmosphere, Journal of Quantitative Spectroscopy and Radiative Transfer, 101, 284–305, https://doi.org/https://doi.org/10.1016/j.jqsrt.2005.11.020, 2006.

https://doi.org/10.5194/egusphere-2025-6328
Preprint. Discussion started: 7 January 2026

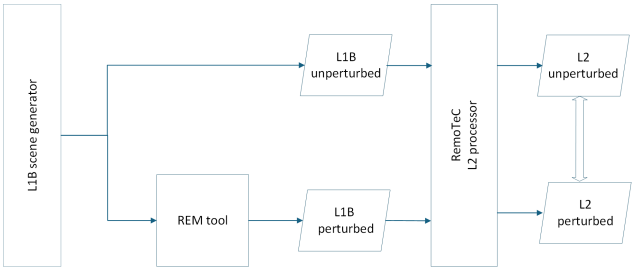

Figure 1. Framework for the simulation experiment with and without persistence perturbation of spectra.

https://doi.org/10.5194/egusphere-2025-6328
Preprint. Discussion started: 7 January 2026

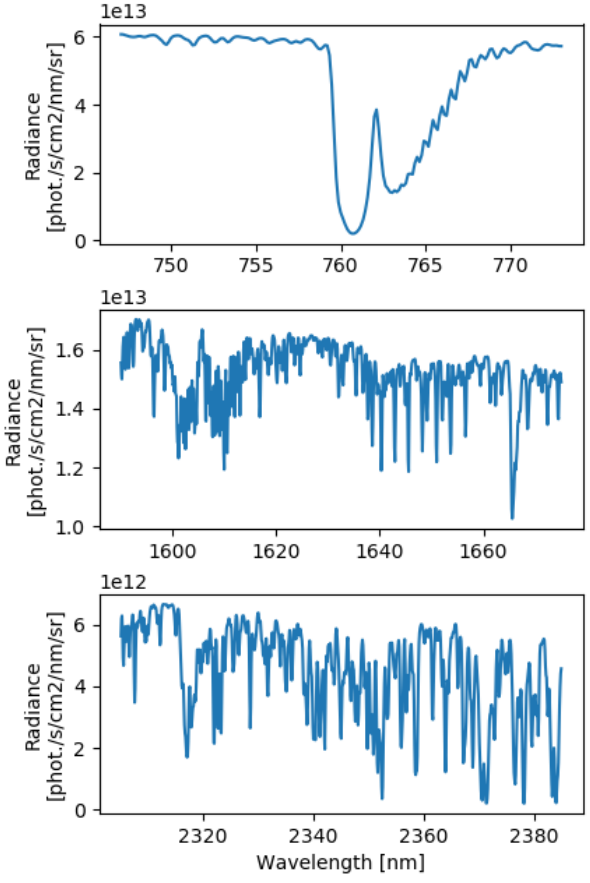

Figure 2. Synthetic reference radiance spectra for the NIR, SWIR-1, and SWIR-3 bands (top to bottom), generated with the LINTRAN V2.1 model in RemoTeC using a constant surface albedo of 0.6 (NIR) and 0.4 (SWIR), and convolving high-resolution solar spectra with the S5 instrument response.

https://doi.org/10.5194/egusphere-2025-6328
Preprint. Discussion started: 7 January 2026

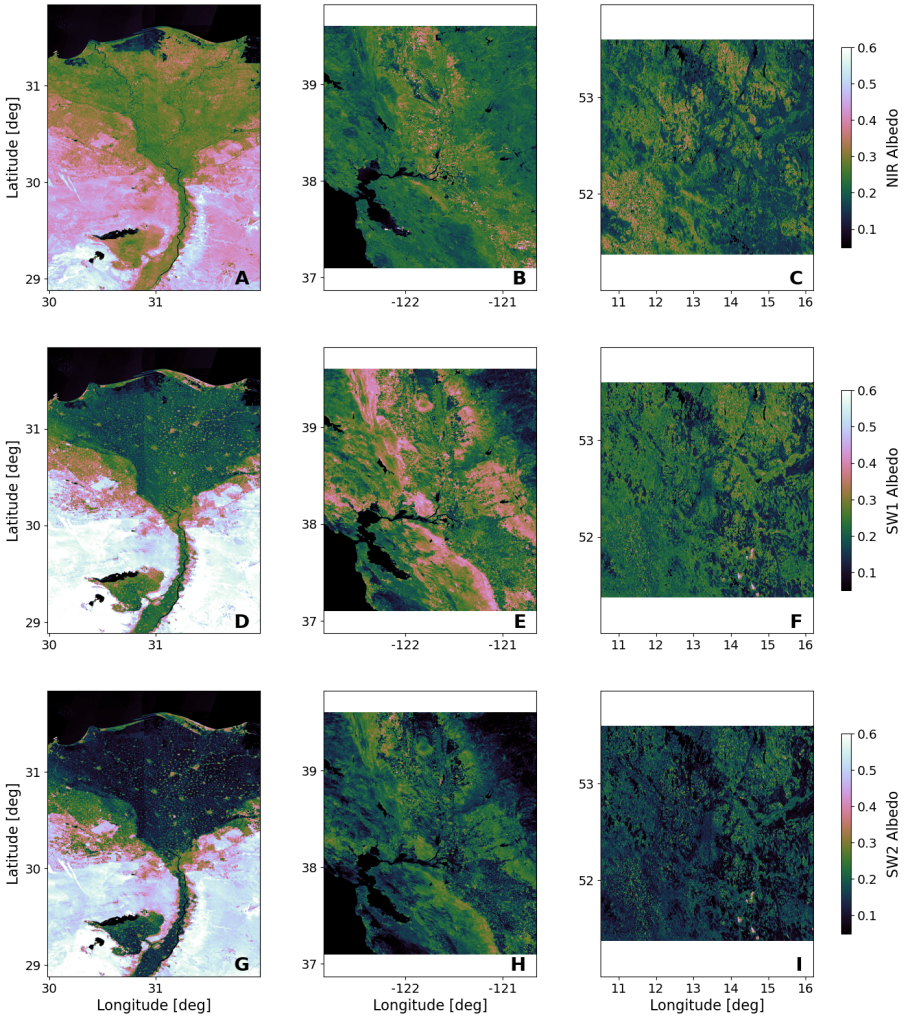

Figure 3. Sentinel-2 albedo scenes for the three selected regions—(A, D, G) Nile Delta, (B, E, H) California's Central Valley, and (C, F, I) the Lusatian lignite district in Germany. The panels show data from the Sentinel-2 bands spectrally closer to Sentinel-5 retrieval windows: (A–C) NIR (mean of bands 6 and 7), (D–F) SWIR-1 (band 10), and (G–I) SWIR-3 (band 11).

https://doi.org/10.5194/egusphere-2025-6328
Preprint. Discussion started: 7 January 2026

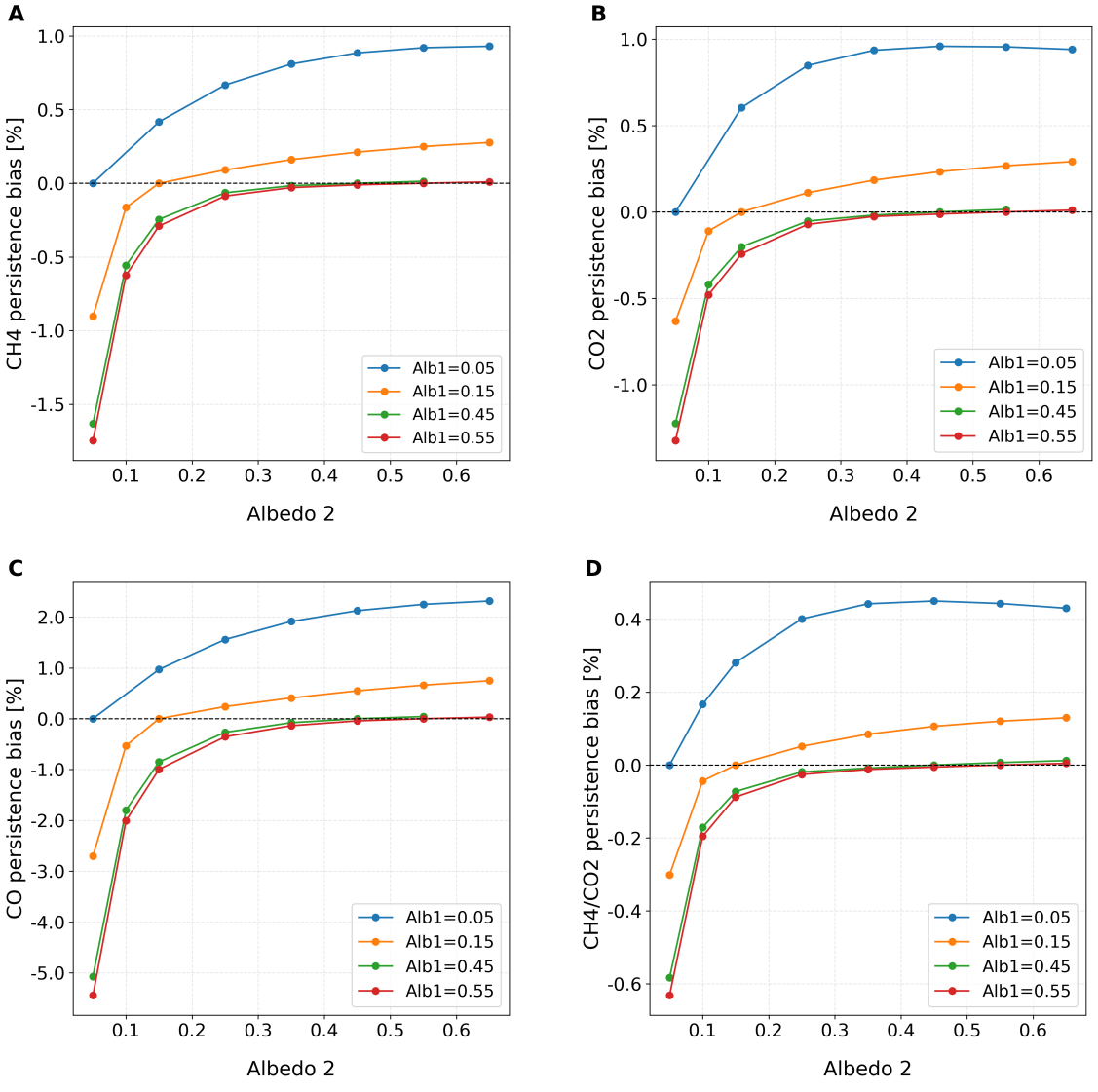

Figure 4. Results for the binary albedo scene with a discontinuity in surface albedo, transitioning from albedo 1 to albedo 2. Panels (A)–(D) show the dependence of the persistence bias on albedo for CH_4, CO_2, CO, and the CH_4/CO_2 proxy retrievals, respectively. Albedo 1 and albedo 2 denote the two albedo values defining the discontinuity. Identical values are used for both SWIR bands, while the NIR albedo is set to 1.5 times the SWIR albedo.

https://doi.org/10.5194/egusphere-2025-6328
Preprint. Discussion started: 7 January 2026

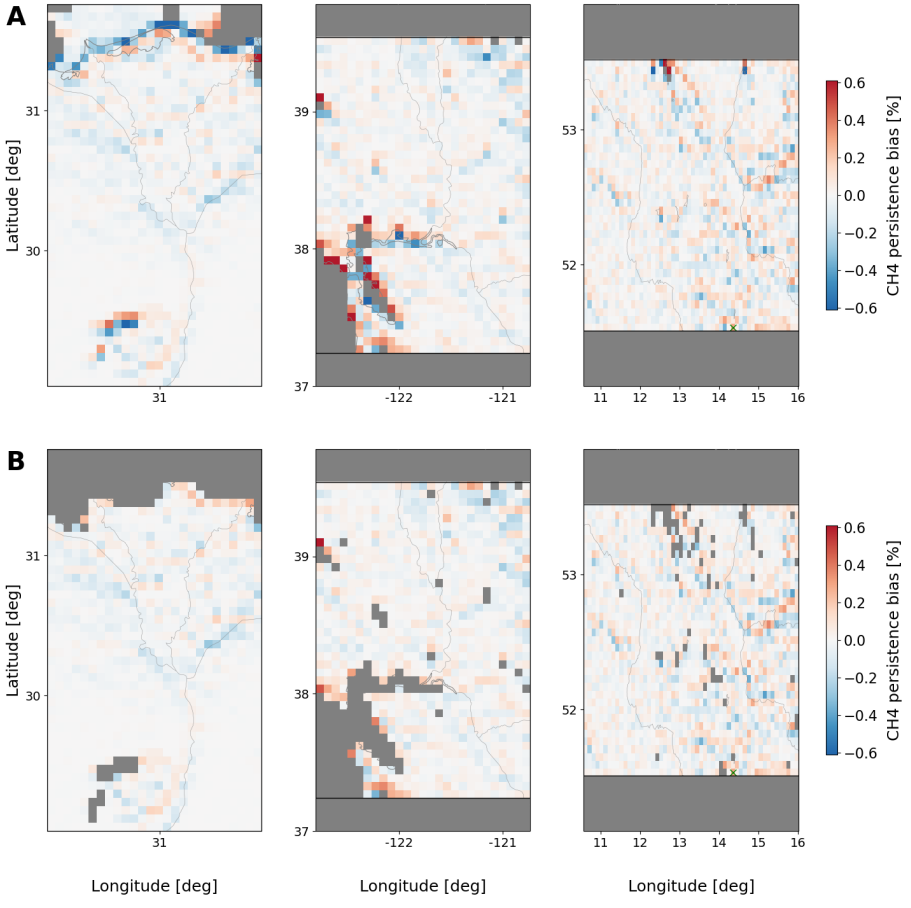

Figure 5. Panels (A) and (B) show CH_4 relative persistence bias maps from the full-physics (scattering) retrieval after applying an albedo threshold filter of 0.05, according to the instrument sensitivity threshold; panel (B) additionally applies a water-land mask. From left to right, the scenes correspond to the Nile Delta, California's Central Valley, and the Lusatian lignite district in Germany. Coastlines, rivers, and lakes are overlaid using Cartopy's built-in Natural Earth features for contextual reference.

https://doi.org/10.5194/egusphere-2025-6328
Preprint. Discussion started: 7 January 2026

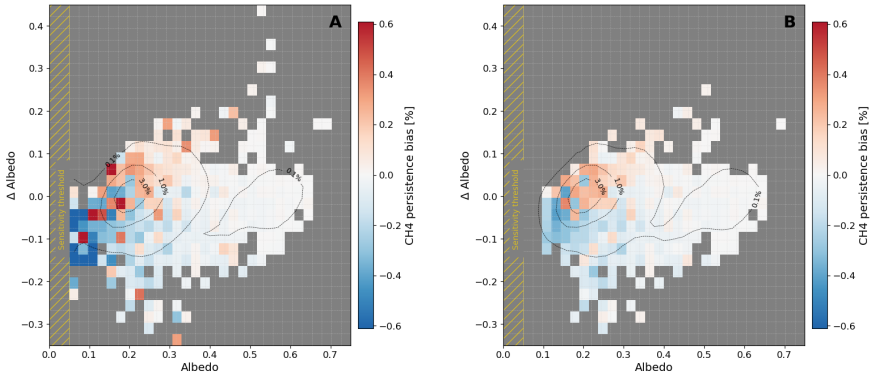

Figure 6. Panel (A) shows the heatmap of the CH_4 relative persistence bias with respect to the SWIR-1 albedo and the corresponding ΔSWIR-1 albedo, after applying an albedo threshold filter of 0.05 consistent with the instrument sensitivity threshold; panel (C) additionally applies a water-land mask. Here, ΔSWIR-1 albedo denotes the difference between the SWIR-1 albedo of a given pixel and that of the preceding pixel along the flight direction. Color indicates the maximum persistence bias in CH_4 across the three combined Sentinel-2 scenes. The gold-shaded region (*albedo* < 0.05) marks the sensitivity threshold of the UVNS spectrometer, where retrieval reliability is reduced. The dotted lines denote the contour plots showing the distribution density of data points within the same (*Albedo*, Δ*Albedo*) parameter space.

https://doi.org/10.5194/egusphere-2025-6328
Preprint. Discussion started: 7 January 2026

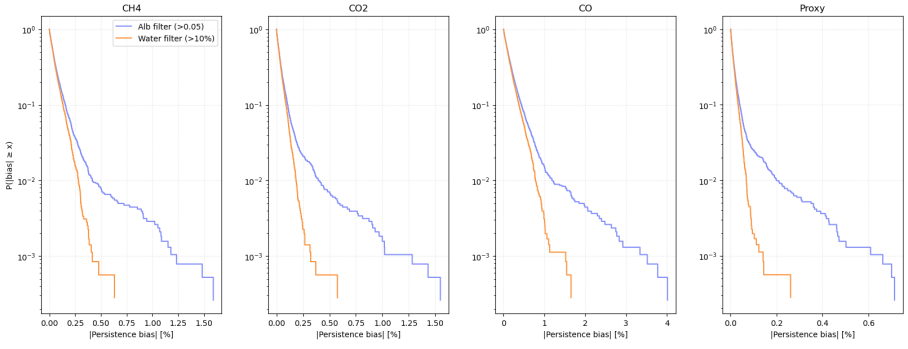

Figure 7. Each panel shows the complementary cumulative distribution function (CCDF) of the absolute persistence bias for CH_4, CO_2, CO, and for the CH_4/CO_2 proxy ratio, combining data from the three Sentinel-2 scenes (the Nile Delta, California's Central Valley, and the Lusatian lignite district in Germany). Blue lines correspond to retrievals filtered with an albedo threshold of 0.05, consistent with the instrument sensitivity limit, while orange lines additionally include the water-land mask. The CCDFs represent the fraction of retrievals with an absolute bias exceeding a given threshold, allowing a direct comparison of the error-distribution tails for the two filter configurations.

https://doi.org/10.5194/egusphere-2025-6328
Preprint. Discussion started: 7 January 2026

Table 1. Statistical overview of persistence-induced retrieval biases before and after applying the land/water mask. Mean, standard deviation, and maximum persistence biases (in %) are shown for each trace gas across the three Sentinel-2 albedo scenes: the Nile Delta, California's Central Valley, and the Lusatian lignite district in Germany. (Top) Statistics after applying an albedo threshold filter of 0.05; (bottom) statistics after additionally applying a land/water mask.

	Nile Delta	California Valley	Lusatian
CH_4	-0.021 / 0.12 / -1.23	0.004 / 0.15 / 1.59	0.000 / 0.11 / 1.07
CO_2	-0.017 / 0.10 / -1.02	0.004 / 0.12 / 1.55	0.002 / 0.08 / 1.28
CO	-0.073 / 0.33 / -3.52	0.015 / 0.40 / 4.01	0.003 / 0.29 / 1.99
Proxy	-0.008 / 0.05 / -0.70	0.002 / 0.06 / 0.71	-0.000 / 0.03 / 0.61
CH_4	-0.009 / 0.05 / -0.31	0.001 / 0.08 / 0.63	0.000 / 0.09 / -0.42
CO_2	-0.007 / 0.04 / -0.32	0.002 / 0.06 / 0.58	0.002 / 0.06 / -0.32
CO	-0.033 / 0.16 / -0.92	0.009 / 0.25 / 1.65	0.006 / 0.27 / -1.13
Proxy	-0.002 / 0.014 / -0.14	0.000 / 0.02 / 0.26	0.000 / 0.02 / -0.14

https://doi.org/10.5194/egusphere-2025-6328
Preprint. Discussion started: 7 January 2026

Table A1. Parameters of the persistence model as derived by CNES for the S5 and MicroCarb detector (Jouglet et al., personal communication) and specifying the S5 SWIR spectrometer.

parameter	description	value	units
Q_E	Quantum efficiency	0.85	e/photons
A	Instrument aperture size		cm^2
Ω	Opening solid angle		sr
T	optical transmission	0.4	-
$\Delta\lambda$	spectral sampling distance	0.1	nm
E_{trap}	trapping efficiency	0.8	-
E_{detrap}	de-trapping efficiency	140	$\mathrm{e/s}$
a	de-trapping coefficient	4.6×10^{-4}	e^{-1}
Q_{max}	maximum trapped charges	16000	e

https://doi.org/10.5194/egusphere-2025-6328
Preprint. Discussion started: 7 January 2026

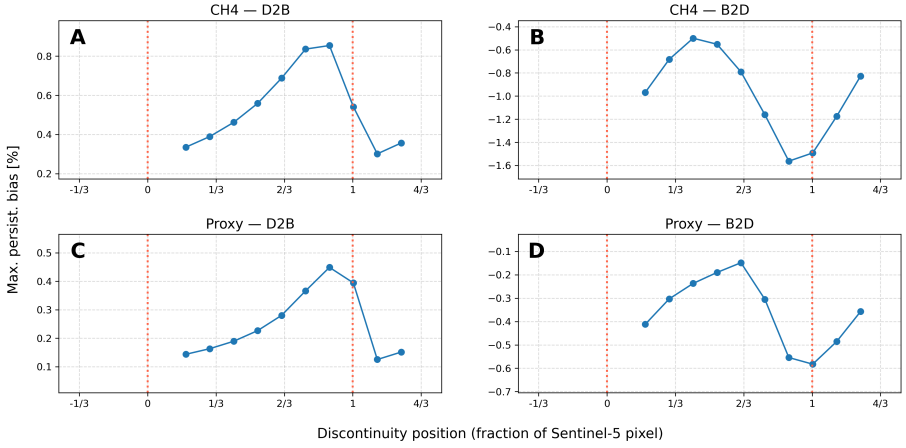

Figure A1. Panels (A) and (B) show the maximum persistence-induced CH_4 bias for the full-physics (scattering) retrieval as a function of the normalized position of the albedo discontinuity within the Sentinel-5 pixel, (0 = pixel start, 1 = pixel end). Panels (C) and (D) show the corresponding CH_4/CO_2 bias for the proxy (non-scattering) retrieval. Panels (A) and (C) refer to the dark-to-bright (D2B) albedo scenes; and panels (B) and (D), to the bright-to-dark (B2D) albedo scenes. Two dotted red lines mark the Sentinel-5 pixel boundaries.

https://doi.org/10.5194/egusphere-2025-6328
Preprint. Discussion started: 7 January 2026

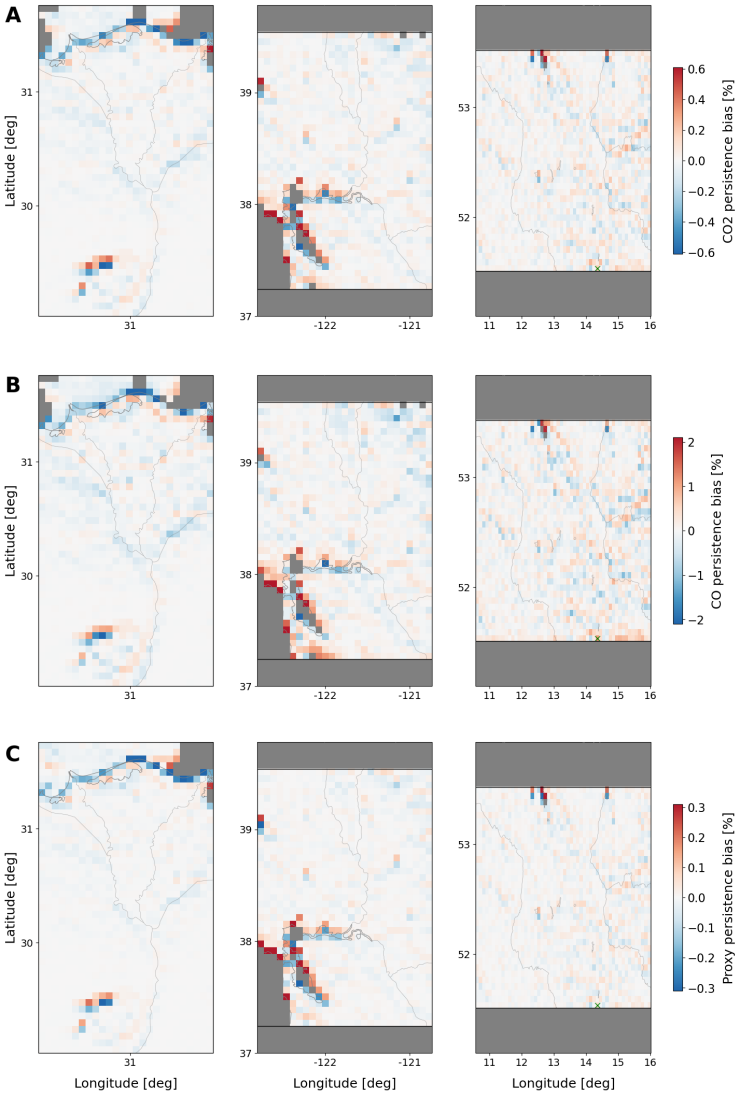

Figure A2. Spatial patterns of relative persistence bias for albedo threshold filtering equal to 0.05. Panels (A) and (B) show persistence bias maps for CO_2 and CO from the full-physics (scattering) retrievals, while plots in panel (C) presents the CH_4/CO_2 ratio from the proxy (non-scattering) retrieval. The maps correspond, from left to right, to scenes over the Nile Delta, California's Central Valley, and the Lusatian lignite district in Germany. Coastlines, rivers, and lakes are overlaid using Cartopy's built-in Natural Earth features for contextual reference.

https://doi.org/10.5194/egusphere-2025-6328
Preprint. Discussion started: 7 January 2026

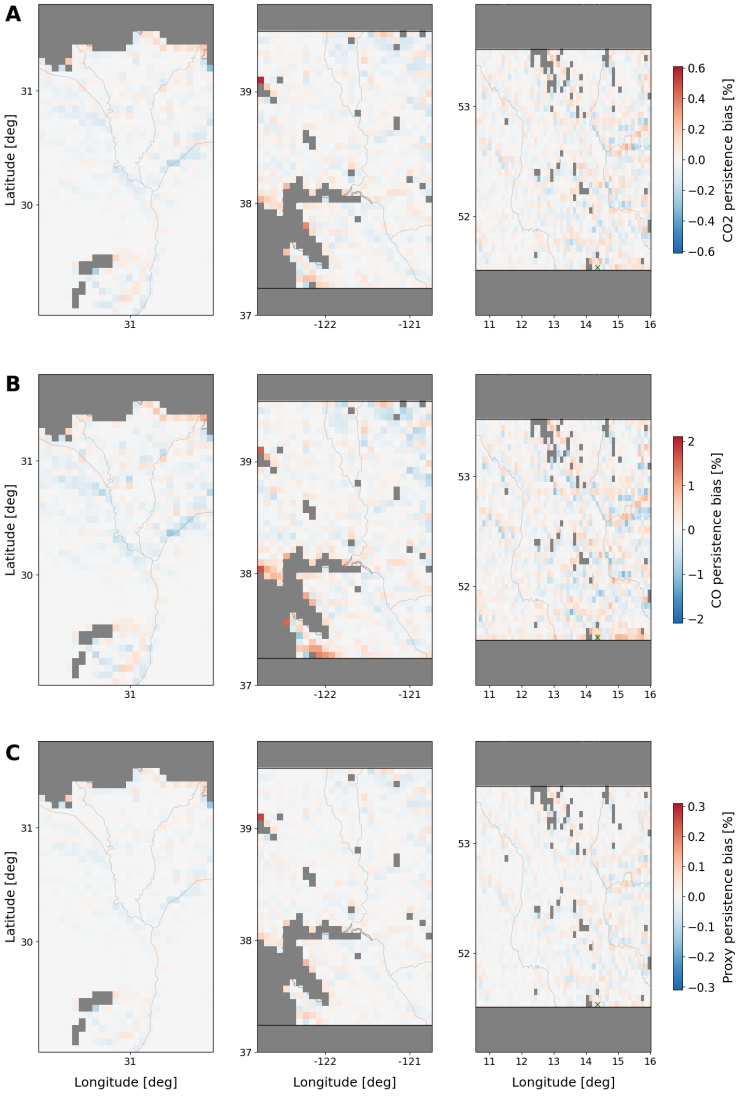

Figure A3. Spatial patterns of relative persistence bias for albedo threshold filtering equal to 0.05 and the water-land mask. Panels (A) and (B) show persistence bias maps for CO_2 and CO from the full-physics (scattering) retrievals, while plots in panel (C) presents the CH_4/CO_2 ratio from the proxy (non-scattering) retrieval. The maps correspond, from left to right, to scenes over the Nile Delta, California's Central Valley, and the Lusatian lignite district in Germany. Coastlines, rivers, and lakes are overlaid using Cartopy's built-in Natural Earth features for contextual reference.

https://doi.org/10.5194/egusphere-2025-6328
Preprint. Discussion started: 7 January 2026

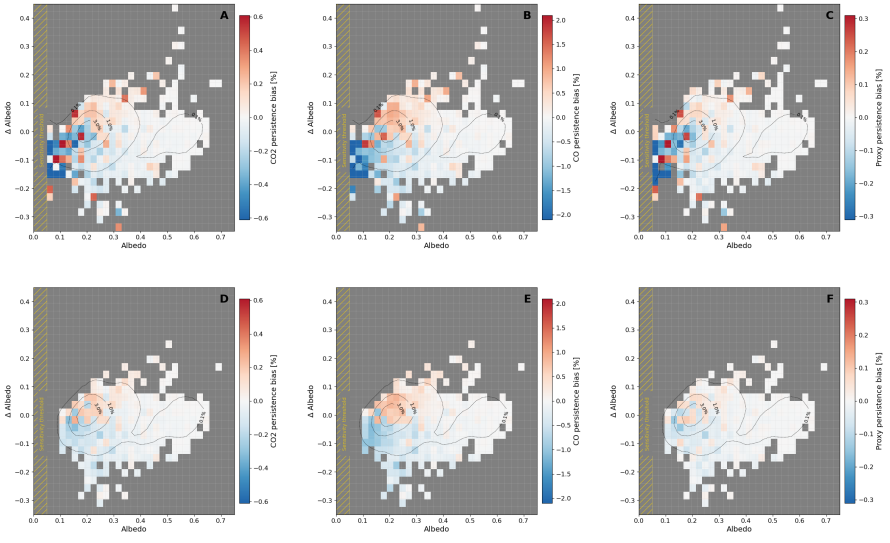

Figure A4. Panels (A-C) show heatmaps of the relative persistence bias with respect to SWIR-1 albedo and the corresponding ΔSWIR-1 albedo, after applying an albedo threshold filter of 0.05 consistent with the instrument sensitivity threshold; panels (C-E) additionally applies a water-land mask. Panels (A-D) and (B-E) corresponds to CO_2 and CO from the full-physics retrievals respectively, while panels (C-F) presents the CH_4/CO_2 ratio from the proxy retrieval. ΔSWIR-1 albedo denotes the difference between the SWIR-1 albedo of a given pixel and that of the preceding pixel along the flight direction. Color indicates the corresponding maximum persistence bias across the three combined Sentinel-2 scenes. The gold-shaded region (*albedo* < 0.05) marks the sensitivity threshold of the UVNS spectrometer, where retrieval reliability is reduced. The dotted lines denote the contour plots showing the distribution density of data points within the same (*Albedo*, Δ*Albedo*) parameter space.